Designing Biphenanthridine-Based Singlet Fission Materials Using Computational Chemistry

Keighlynn A. Veilleux, Georg Schreckenbach, David E. Herbert**

Department of Chemistry and the Manitoba Institute for Materials, University of Manitoba, 144 Dysart Road, Winnipeg, MB R3T 2N2, Canada

*schrecke@cc.umanitoba.ca; david.herbert@umanitoba.ca

ABSTRACT

Singlet fission has the potential to significantly improve the efficiency of photovoltaic devices by harnessing high-energy sunlight to double the photocurrent that can be generated in standard semiconductors. The challenge is identifying materials capable of undergoing this process efficiently. Herein, we present the results of a systematic search for novel intermolecular singlet fission materials based on the recently synthesized 6,6'-biphenanthridine (biphe) framework utilizing a straightforward computational approach. Density functional theory (DFT) and time-dependent density functional theory (TD-DFT) were employed to study the photophysics of various structural analogues of biphe. These analogues were generated *in silico* by utilizing an extensive range of transformations, including planarization, protonation, symmetric and asymmetric alkylation, electron-donating and electron-withdrawing group substitution, *N*-oxide substitution, and symmetric and asymmetric π-extension and contraction. Analysis of the effects of these structural modifications on the energies of the lowest singlet and triplet excited states revealed that (2,2',10,10'-tetra-*N*-oxide) planar biphe has an $E(S_1)/E(T_1)$ ratio of 2.12 and an $E(T_2)/E(T_1)$ of 2.05, suggesting its potential for intermolecular singlet fission. Additionally, *N*-methylated biphe emerged as a promising contender for thermally activated delayed fluorescence. The effects of solvation are also discussed.

INTRODUCTION

The efficiencies of photovoltaic (PV) devices are fundamentally limited by thermodynamics. In conventional semi-conductor PV devices, photons with energies less than the semiconductor's band gap are not absorbed, while the excess energy of photons with energies greater than the band gap is lost as heat. The combination of these and other losses result in a maximum theoretical photoelectric conversion efficiency of ~32% for a single-junction solar cell.[1] Singlet fission (SF) provides a promising means to overcoming this limit by exploiting multiple exciton generation to produce two excited electrons from each photon absorbed. In this process, non-radiative decay of an excited singlet state of one chromophore into a triplet state induces the excitation of a neighbouring chromophore into its triplet state.[2] Thus, the excitation energy of one initial excited singlet state is distributed to form two lower-lying triplets, effectively doubling the current that can be generated in a photovoltaic cell compared to ordinary photoelectric conversion. Moreover, by absorbing higher-energy photons of the solar spectrum compared to conventional semiconductors,[3] combining SF chromophores with conventional semiconductors can significantly improve overall photoelectric conversion efficiencies by increasing the range of frequencies of light that can be productively harvested. Organic solar cells that incorporate the canonical SF material pentacene have accordingly achieved external quantum efficiencies of up to 126% and internal quantum efficiencies around 160%.[3,4] Beyond photovoltaics, SF materials have potential applications in quantum information science[5] and in nuclear magnetic resonance experiments as polarized spin generators,[6] explaining the wide interest in the design of novel SF chromophores.

Efficient SF requires that the energy of the initially generated singlet excited state (S_1) be at least twice that of the lowest-lying triplet state (T_1; Figure 1a).[2,7] Ideally, the $E(S_1)/E(T_1)$ ratio

should be only slightly greater than two, given that an excessively exoergic process would slow down SF rates and may promote other decay pathways.[8] In addition, the energy of the second lowest triplet state (T_2) must also be at least twice that of T_1 to ensure that two T_1 states do not recombine to form a T_2 state in a single chromophore (leaving the other in its ground state, S_0)[2,7] as this excited state can undergo rapid internal conversion back to T_1, losing energy in the form of heat.[9] Satisfying both these conditions ensures an exoergic (or at least isoergic) process. With particular respect to applications involving silicon-based solar cells, forming a triplet state in a SF material that is 1.2 to 1.5 eV above the ground state [$E(S_0) = 0$ eV] would help obviate additional energy losses.[10,11] When these energetics are all favourable, SF can occur on a sub-ps timescale.[12] Formation of a correlated triplet pair, $^1(T_1T_1)$, may occur through a direct two-electron process or involve intermediary charge transfer (CT) states, wherein the excited electron of chromophore A moves to chromophore B before an electron of opposite spin is transferred from B to A (Figure 1b). The final step of SF is the decoupling of this triplet pair to form two independent triplets, the rate of which can be highly system-dependent.[13]

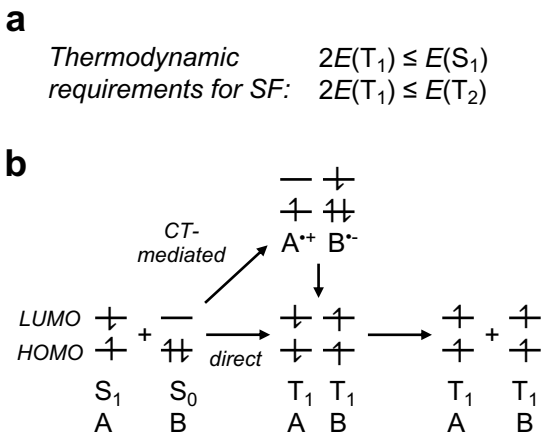

Figure 1. (a) Thermodynamic requirements for efficient SF; (b) electronic configurations involved in SF with both a direct and a charge-transfer (CT) mediated pathway shown. A and B denote the two chromophores.

Due to these energetic constraints, the number of molecules known to undergo SF is rather limited. The most well-studied SF chromophores are those based on acenes, such as pentacene and tetracene.[14] However, a major limiting factor in the potential application of linear acenes is their poor chemical stabilities.[8] We recently developed methods for synthesizing dimers of phenanthridine (**1**; benzo[*c*]quinoline), namely 6,6'-biphenanthridine (biphe, **2**; Figure 2).[15] Phenanthridine is a fluorescent *N*-heterocycle with two benzo rings fused asymmetrically to a pyridine core. Phenanthridine appears in the DNA intercalative dyes ethidium bromide,[16] anti-neoplastic platinum coordination compounds (e.g., phenanthriplatin (*cis*-$[Pt^{II}(NH_3)_2(\text{phenanthridine})Cl]NO_3$)[17] and has been used as a co-catalyst in transfer hydrogenation reactions.[18,19] To date, we have mainly explored the use of phenanthridine in the context of coordination chemistry, with a focus on photophysical applications.[20]

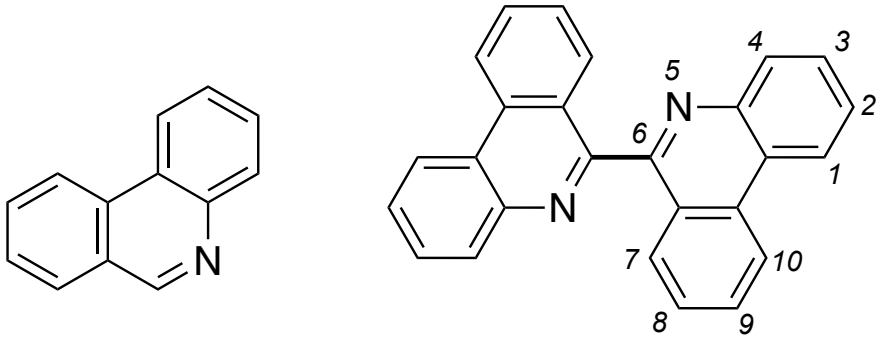

Figure 2. Structure of phenanthridine (**1**) and 6,6'-biphenanthridine (biphe; **2**) with the IUPAC numbering scheme shown in italics.

Importantly, due to the significant twist of the adjoining C-C bond in **2**, the two covalently linked phenanthridinyl subunits are not conjugated in the ground state. As such, they are able to function as distinct chromophores. This prompted us to consider if intramolecular SF via coupling

of the excited states across the connecting C-C single bond which exhibits π-bonding character in the LUMO might be feasible. Alternatively, chemical modifications of **2** that conjugate both phenanthridinyl sub-units may yield a single molecular chromophoric entity with the right energetics for intermolecular SF. Here, we use computational methods to evaluate certain photophysical properties of a library of biphe analogues including planarized structures. In particular, the energies of the lowest excited singlet and triplet states were calculated relative to the ground state allowing insight into how synthetically feasible structural modifications influence the critical energetic ratios $E(S_1)/E(T_1)$ and $E(T_2)/E(T_1)$, in an effort to identify candidate SF materials.

COMPUTATIONAL METHODS

All calculations were carried out using ORCA v5.0.4,[21–23] and performed in the gas phase unless otherwise specified. Select molecules were also studied in solution using the implicit solvation model SMD.[24] The following convergence criteria and DFT grids were used: optimization - tightopt, tightscf, defgrid3; single points - tightscf, defgrid2; TD-DFT: tightscf, defgrid3. The ground-state (S_0) geometry of each structure was optimized using the PBE0[25,26] functional with D3BJ[27] dispersion correction and the def2-SVP[28] basis set. Frequency calculations were performed to confirm the absence of imaginary frequencies, indicating that each optimized structure is at a true minimum on the potential energy surface. Vertical excitation energies for the three electronic transitions of interest ($S_0 \rightarrow S_1$; $S_0 \rightarrow T_1$; $S_0 \rightarrow T_2$) were calculated using TD-DFT to approximate the S_1, T_1, and T_2 energies with respect to the ground state [$E(S_0) = 0$ eV]. Single-point energy and TD-DFT calculations were performed using the O3LYP[29] functional with the def2-TZVP[28] basis set and the RIJCOSX approximation[30–32] employing the auxiliary basis set def2/J.[33] TD-DFT calculations implemented the Tamm-Dancoff approximation[34] which avoids triplet instabilities common to TD-DFT calculations.[35] The level of theory employed in this study (TD-RIJCOSX-O3LYP/def2-TZVP+def2/J//PBE0-D3(BJ)/def2-SVP) has previously shown good agreement with the experimental crystal structure of biphe and the ultraviolet-visible absorption spectra of both biphe and protonated biphe when used with SMD.[15] Additionally, we believe our approach is reasonable since we are primarily interested in identifying trends, rather than precise numerical values. Ground-state molecular orbital (MO) isosurfaces were generated using the molecular editor Chemcraft v1.8[36] and are visualized throughout using contour values of 0.03.

RESULTS AND DISCUSSION

The molecular structures studied in this work (**1**-**53**) are presented in Chart 1. The selected structures represent a range of molecular motifs that target two major directions in SF chromophore design. First, the influence of planarization in biphenanthridine frameworks was investigated. Coplanar conformation of the two halves of **2** is prevented by steric clashing between the hydrogen atoms at the 7 and 7' positions.[15] Covalently bonding carbon 7 and carbon 7' to form **5** induces a planar geometry which is predicted to cause an increase in the π-bonding character across the C(6)-C(6') bond in the LUMO observed in **2**, due to greater overlap of the C7/C7' 2p orbitals. Second, theoretical modeling of charge-transfer mediated SF in covalent dimers suggests that breaking the symmetry of a homodimer can enhance SF yields by reducing the destructive quantum interference between left and right localized S_1 electron configurations and CT configurations.[37] Modifications such as protonation (**3** and **6**), *N*-alkylation (**4** and **7**), or the addition of electron-withdrawing (EWG) or electron-donating (EDG) substituents to a symmetric parent molecule were therefore included so as to break symmetry and potentially unlock a charge-transfer mediated mechanism of SF. In addition, the doubly *N*-alkylated structures **8** and **9** were also considered which are symmetric, bearing a C_2 axis as drawn.

Our initial study of biphe (**2**) showed that mono-protonation to form **3** causes substantial localization of the highest occupied and lowest unoccupied MOs (HOMO and LUMO, respectively) on different phenanthridinyl subunits, lending the HOMO→LUMO transition significant charge-transfer character.[15] Selective placement of functional groups (EDG: NH_2, NMe_2; EWG: CF_3, NO_2) or combinations thereof (**10**-**40**) with an eye to bringing about push-pull effects on the electron density that might facilitate charge-transfer mediated SF were examined using the planar framework of **5**. Taking inspiration from recent work on small intramolecular SF

chromophores,[38] some analogues of **5** incorporating *N*-oxide groups (**41**-**45**) were studied. Finally, the impact of further symmetric or asymmetric π-extension (**46**-**51**) or contraction (**52**-**53**) was probed.

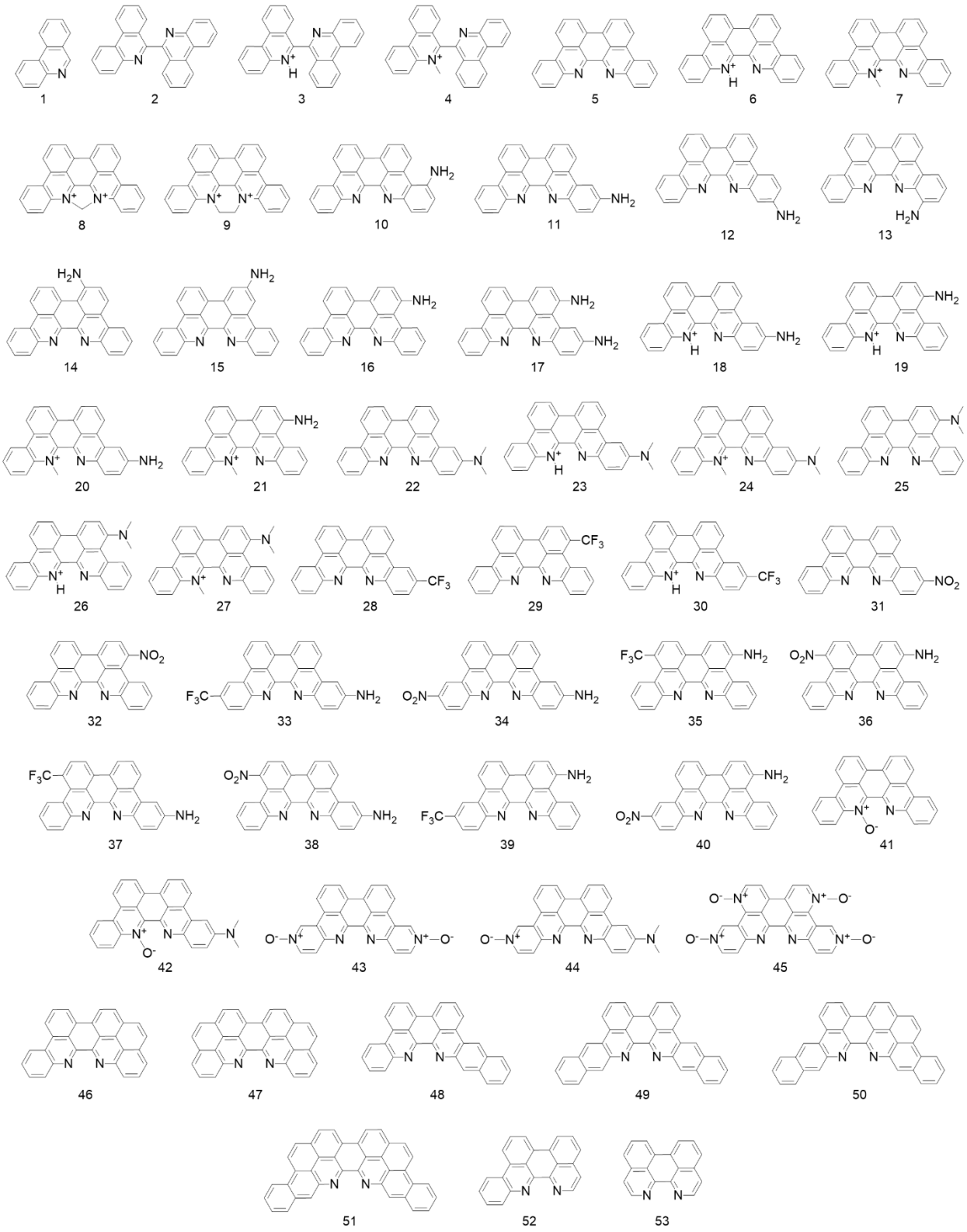

Chart 1. Structures considered in this work.

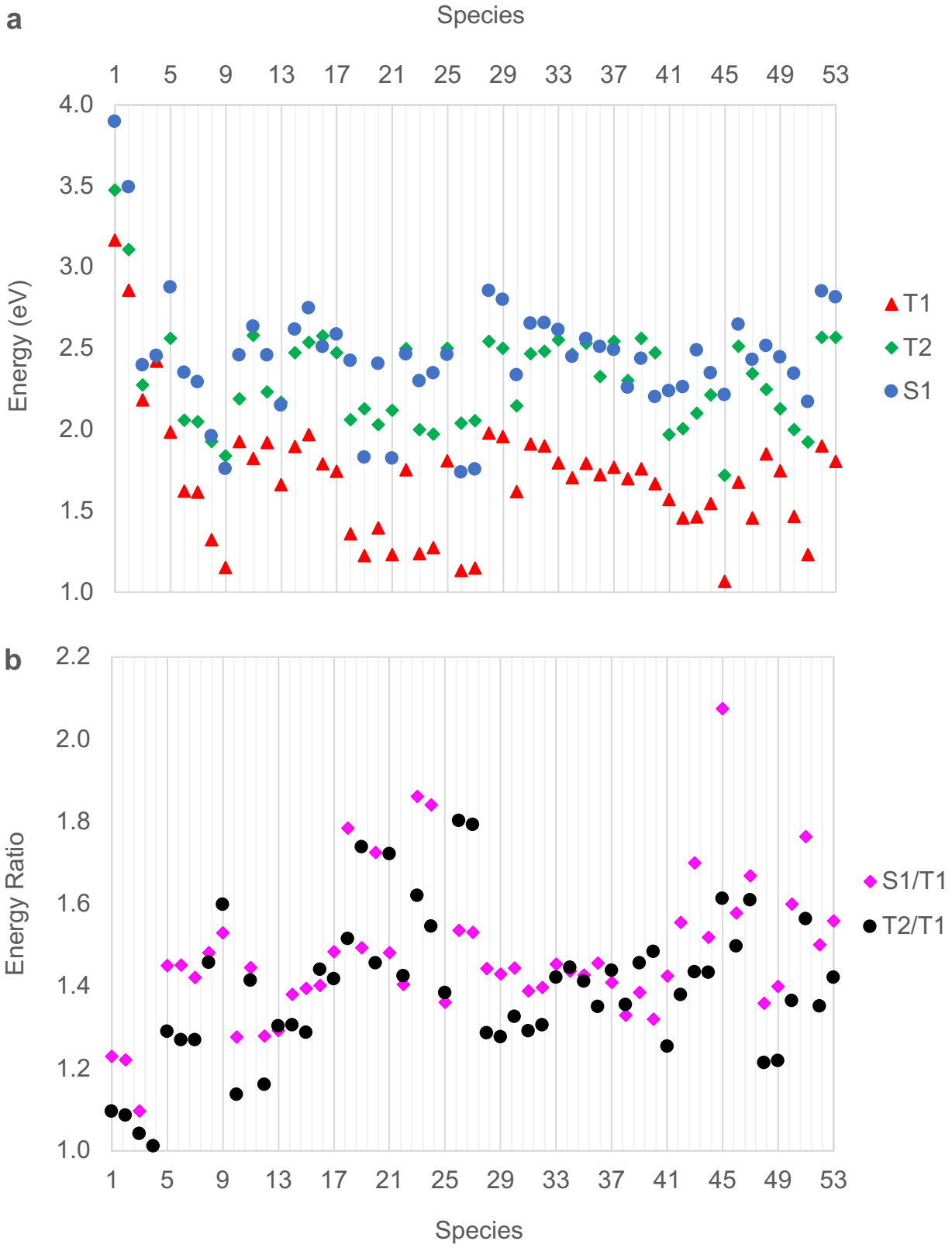

Figure 3. (a) Calculated excitation energies; (b) calculated excitation energy ratios.

Table 1. Calculated excited state energies and their ratios of gas-phase structures.

Structure	$E(T_1)$ / eV	$E(S_1)$ / eV	$E(T_2)$ / eV	$\frac{E(S_1)}{E(T_1)}$	$\frac{E(T_2)}{E(T_1)}$
1	3.17	3.90	3.48	1.23	1.10
2	2.86	3.49	3.11	1.22	1.09
3	2.18	2.40	2.28	1.10	1.04
4	2.42	2.46	2.45	1.01	1.01
5	1.98	2.88	2.56	1.45	1.29
6	1.62	2.35	2.06	1.45	1.27
7	1.61	2.30	2.05	1.42	1.27
8	1.32	1.96	1.93	1.48	1.46
9	1.15	1.76	1.84	1.53	1.60
10	1.93	2.46	2.19	1.28	1.14
11	1.82	2.64	2.58	1.45	1.42

12	1.92	2.46	2.23	1.28	1.16
13	1.66	2.15	2.17	1.29	1.30
14	1.90	2.62	2.48	1.38	1.31
15	1.97	2.75	2.54	1.40	1.29
16	1.79	2.51	2.58	1.40	1.44
17	1.74	2.59	2.47	1.48	1.42
18	1.36	2.43	2.06	1.78	1.52
19	1.23	1.83	2.13	1.49	1.74
20	1.39	2.41	2.03	1.73	1.46
21	1.23	1.82	2.12	1.48	1.72
22	1.75	2.46	2.50	1.40	1.43
23	1.24	2.30	2.00	1.86	1.62
24	1.28	2.35	1.97	1.84	1.55

25	1.81	2.46	2.50	1.36	1.38
26	1.13	1.74	2.04	1.54	1.80
27	1.15	1.76	2.06	1.53	1.79
28	1.98	2.86	2.54	1.44	1.29
29	1.96	2.80	2.50	1.43	1.28
30	1.62	2.34	2.15	1.44	1.33
31	1.91	2.65	2.47	1.39	1.29
32	1.90	2.66	2.48	1.40	1.31
33	1.80	2.61	2.55	1.45	1.42
34	1.71	2.45	2.47	1.44	1.45
35	1.79	2.56	2.53	1.43	1.41
36	1.72	2.51	2.33	1.46	1.35
37	1.77	2.49	2.54	1.41	1.44

38	1.70	2.26	2.30	1.33	1.36
39	1.76	2.44	2.56	1.39	1.46
40	1.67	2.20	2.48	1.32	1.48
41	1.57	2.24	1.97	1.43	1.25
42	1.46	2.26	2.01	1.56	1.38
43	1.46	2.49	2.10	1.70	1.44
44	1.54	2.35	2.21	1.52	1.43
45	1.07	2.21	1.72	2.08	1.61
46	1.68	2.65	2.51	1.58	1.50
47	1.46	2.43	2.35	1.67	1.61
48	1.85	2.52	2.25	1.36	1.21
49	1.75	2.45	2.13	1.40	1.22
50	1.46	2.34	2.00	1.60	1.37

51	1.23	2.17	1.92	1.76	1.56
52	1.90	2.85	2.57	1.50	1.35
53	1.81	2.82	2.57	1.56	1.42

The results of the energy estimates for the gas-phase excited states S_1, T_1 and T_2, and the two key energy ratios ($E(S_1)/E(T_1)$, $E(T_2)/E(T_1)$) are provided in Table 1 and depicted graphically in Figure 3. Looking first at phenanthridine (**1**) and biphe itself (**2**), we see that the critical energetic ratios are largely unaffected by dimerization, in keeping with our expectation that **2** contains two separate chromophores. However, the excited states of **2** are notably more stabilized than those of **1** due to greater delocalization of the π system in the excited states of the dimer. This is evinced by the orbital structure of the LUMO of **2** which, as discussed above, indicates π-bonding character across the connecting C-C bond (Figure 4). We next discuss the impacts of each aforementioned structural modification in turn.

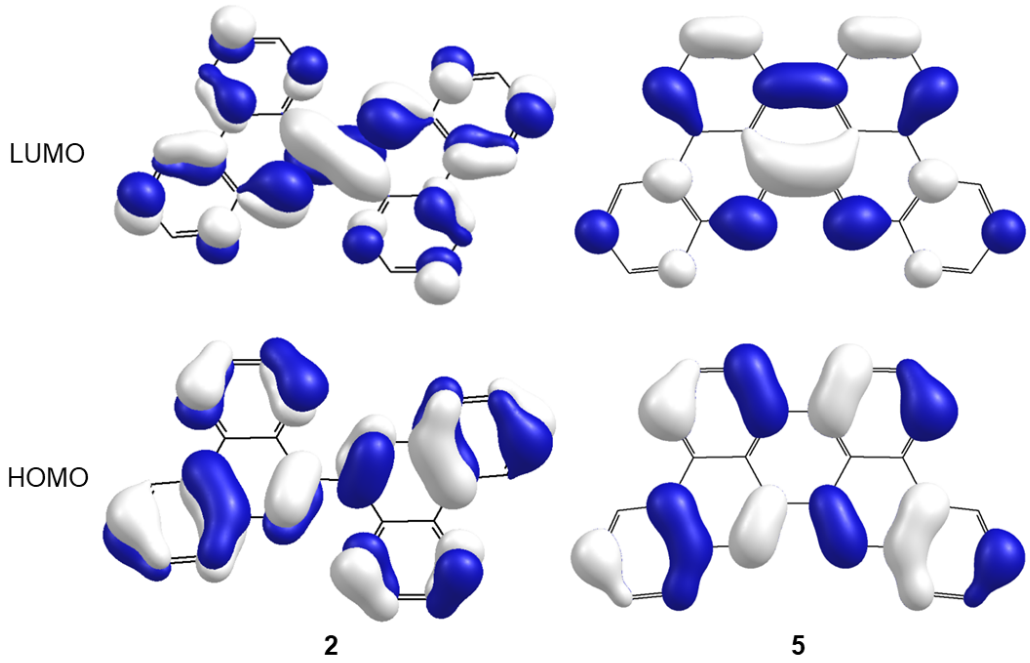

Figure 4. Frontier molecular orbitals of **2** and **5**. The blue and white shading represents the two phases of the wave function.

Planarization. Planar biphe (**5**) has significantly stabilized excited states relative to **2**. Of the three calculated excited states, the T_1 state is stabilized the most (-0.88 eV), followed by S_1 (-0.61 eV), then T_2 (-0.55 eV); thus, both energetic ratios were improved upon planarization of **2** which may be a simple consequence of planarization forming a larger π-system through combining the two phenanthridine halves. Indeed, planar **5** was found to have both greater π-bonding character in its LUMO and greater π-antibonding character in its HOMO across the linking C(6)-C(6') bond which is 0.014 Å shorter than that of **2**. The orbital character of the frontier MOs at the newly formed C(7)-C(7') bond is notably similar to that at the C(6)-C(6') bond. Importantly, the HOMO-29 (Figure S1) exhibits π-bonding across the two phenanthridinyl sub-units, consistent with ground state conjugation of the two π systems. This suggests that an intramolecular mechanism of SF is not feasible for planar biphe analogues (e.g., **5**). Nonetheless, our analysis of excited state energies provides a preliminary screening to identify potential intermolecular SF chromophores.

Protonation. Protonation of both **2** and **5** to form **3** and **6**, respectively, was observed to differentially stabilize the excited states of interest. The S_1 state of protonated biphe (**3**) is stabilized significantly more than the triplet states compared to those in **2**, leading to a reduction in the $E(S_1)/E(T_1)$ ratio (-0.12); $E(T_2)/E(T_1)$ also slightly decreased (-0.05). Protonation of **5** had a smaller effect on these energetic ratios such that the $E(S_1)/E(T_1)$ ratio of protonated planar biphe (**6**) remained the same as for unprotonated **5**, while $E(T_2)/E(T_1)$ decreased slightly (-0.02). Looking at the vertical excitations, the $S_0 \rightarrow S_1$ transition of **3** is 95% HOMO→LUMO in character but has a considerably smaller oscillator strength compared to the $S_0 \rightarrow S_2$ transition which is primarily HOMO-1→LUMO in character (91%) (Table S1). Both the HOMO and HOMO-1 of **3** (Figure 5) are highly localized on the non-protonated phenanthridinyl subunit, whereas the LUMO is mostly concentrated on the protonated subunit. This indicates that both the $S_0 \rightarrow S_1$ and the $S_0 \rightarrow S_2$ excitation should have significant CT character. The LUMO of **3** also retains some of the π-bonding character across the C(6)-C(6') bond that is seen in **2**. In comparison, the $S_0 \rightarrow S_1$ transition of **6** is 67% HOMO→LUMO and 24% HOMO-1→LUMO. Unlike its non-planar counterpart, only minor asymmetry can be seen in the frontier MOs of **6** (Figure S3). While protonation shortened the C(6)-C(6') bond length of **2** by 0.009 Å, protonation of **5** shortened this bond considerably more (by 0.027 Å). Additionally, the N-H bond lengths of the protonated imine of **3** and **6** are 1.024 Å and 1.027 Å, respectively. The shorter C(6)-C(6') bond length and longer N-H bond length of **6** relative to **3** suggest some hydrogen bonding character in the planar analogue, with an N---H separation of 2.154 Å and a 107.0° N-H---N bond angle.

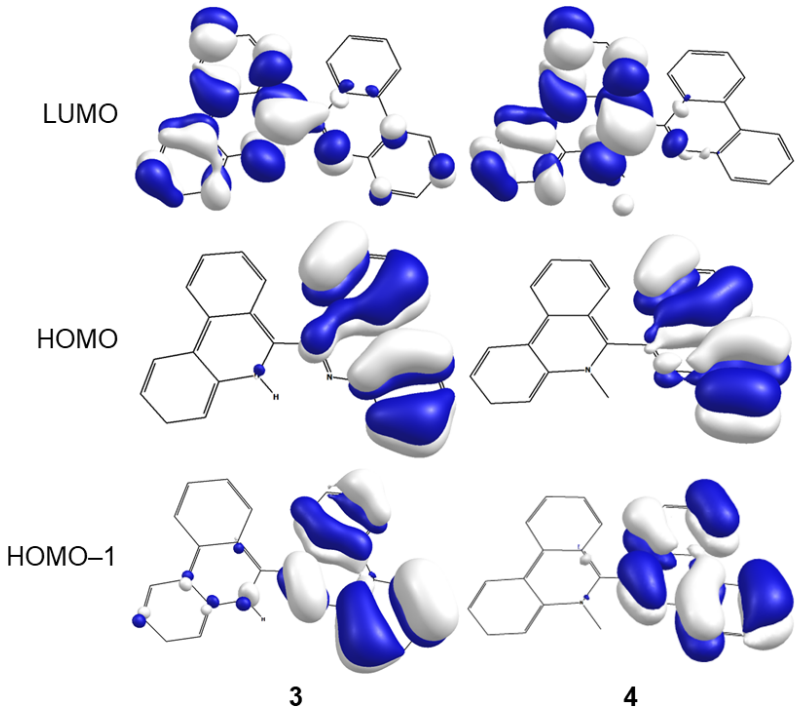

Figure 5. Selected molecular orbitals of **3** and **4**. The blue and white shading represents the two phases of the wave function.

***N*-Alkylation.** Compared to protonation, *N*-methylation of **2** to form the cationic species **4** had less of a stabilizing effect on the excited states relative to S_0. However, the S_1 state was once again lowered the most in energy (ΔE = -1.03 eV) followed by T_2 (ΔE = -0.66 eV), leading to an even greater reduction of $E(S_1)/E(T_1)$ and $E(T_2)/E(T_1)$. The resulting $\Delta E_{S1\text{-}T1}$ (0.034 eV) and $\Delta E_{S1\text{-}T2}$ (0.005 eV) are remarkably small, suggesting that **4** may be a promising candidate for thermally activated delayed fluorescence (TADF).[39] The $S_0 \rightarrow S_1$ transition of **4** is mostly attributed to a HOMO→LUMO excitation (86%) with a 14% contribution from the HOMO-1→LUMO. The slightly stronger $S_0 \rightarrow S_2$ transition is 85% HOMO-1→LUMO and 14% HOMO→LUMO. Similar to **3**, the HOMO and HOMO-1 of **4** remain heavily localized on the non-methylated phenanthridinyl subunit while the LUMO is mostly concentrated on the opposite side of the dimer. Unlike for **2** and **3**, the LUMO of **4** primarily exhibits non-bonding character with respect to the

C(6)-C(6') bond. *N*-Methylation of **5** to produce **7** had similar effects to that of protonation of **5** but with a slightly greater stabilization of the S_1 state relative to **6**. This serves to reduce the $E(S_1)/E(T_1)$ ratio by 0.03 relative to both **5** and **6**. The $S_0 \rightarrow S_1$ transition of *N*-methylated planar biphe (**7**) is mostly HOMO→LUMO (77%) with 13% HOMO-1→LUMO character. Again, minor asymmetry is seen in the frontier MOs of **7** (Figure S3). Methylation also caused significant geometric distortion due to steric effects. While methylation of **2** had a negligible effect on the C(6)-C(6') bond length, methylation of **5** reduced this distance by 0.013 Å. **7** also has a slightly shorter C(7)-C(7') bond length than either **5** or **6**, and shows an increase of 16.4° in the N(5)-C(6)-C(6')-N(5') dihedral angle. On a practical level, this reduction in planarity could help solubilize **7** by disrupting π-π stacking.

Bridging the two phenanthridine nitrogens to generate doubly *N*-alkylated structures **8** (via a one-carbon methylenyl bridge) and **9** (via a two-carbon ethylenyl bridge) was also probed. Unlike mono-methylated analogues, these structures retain C_2 symmetry; **8** also has a mirror plane (C_{2v}) lacking in **9** due to significant twisting (shown in Figure S4). Compared with **5**, a substantial stabilization of each of the excited states relative to S_0 was observed. The $E(S_1)/E(T_1)$ ratio saw minor improvement (+0.03 in **8**; +0.08 in **9**), while the $E(T_2)/E(T_1)$ ratio notably increased relative to **5**, particularly in **9** (+0.17 in **8** vs +0.31 in **9**). The $S_0 \rightarrow S_1$ transition is dominated by the frontier orbitals in both **8** and **9** (85% and 88% HOMO→LUMO, respectively). The HOMOs of **8** and **9** do not comprise the bridging saturated carbons but do show a small degree of π-antibonding character across the C(6)-C(6') bond and strongly π-antibonding character across the C(7)-C(7') bond (Figure S4). The LUMO of each has π-bonding character across the C(6)-C(6') and C(7)-C(7') bonds. Perhaps unsurprisingly due to the inclusion of a short single-carbon bridge, **8** has a much shorter C(6)-C(6') distance compared to **5** (Δd = -0.078 Å) while the C(7)-C(7') bond length

is consequently elongated by 0.011 Å. These bond lengths are 0.011 and 0.012 Å shorter, respectively, in the more flexibly bridged **9** compared to **5**. The N(5)-C(6) bond lengths in both **8** and **9** are significantly longer than in **5** (by 0.025 and 0.042 Å, respectively). **9** also has a substantial 13.8° N(5)-C(6)-C(6')-N(5') dihedral angle compared to the planar structures of **5** or **8**, resulting in a loss of mirror plane symmetry as noted above.

Electron-donating group substitution. At most positions, addition of an electron-donating amino (NH_2) substituent had a detrimental effect on both energetic ratios. Amongst the mono-aminated structures, (4-amino) planar biphe (**13**) had the lowest-energy T_1, S_1, and T_2 states, while (9-amino) planar biphe (**15**) had the highest S_1 energy, followed by (2-amino) planar biphe (**11**) and (8-amino) planar biphe (**14**). Although the $E(S_1)/E(T_1)$ ratio of **11** was found to be isoenergetic to the unsubstituted **5**, the T_1 state was stabilized while T_2 was not, improving $E(T_2)/E(T_1)$ by 0.12. A similar effect was found for (10-amino) planar biphe (**16**), where $E(T_2)/E(T_1)$ was also increased by 0.15, but $E(S_1)/E(T_1)$ decreased by 0.05 relative to **5** attributable to a lower-energy S_1 state. Carbons 1 and 3 were found to be the positions of substitution *least* conducive to the desired SF energetics, yielding particularly low $E(S_1)/E(T_1)$ and $E(T_2)/E(T_1)$ ratios compared to structures with other substitution patterns. While the LUMOs of all the mono-aminated structures are similarly distributed, the HOMOs of 1-amino substituted **10**, 3-amino substituted **12**, and 4-amino-substituted planar biphe (**13**) are more localized on the aminated phenanthridinyl subunit (Figures S5 and S6). These three structures also have, of the series, the lowest energy S_1 and T_2 states.

Given that adding a nitrogen-containing substituent at carbons 2 and 10 yielded the highest energetic ratios among the mono-aminated structures, we also looked at (2,10-diamino) planar biphe (**17**) to investigate the combined effects of substitution at both positions. **17** has lower-energy triplet states than either mono-aminated equivalent, leading to a slightly higher $E(S_1)/E(T_1)$ ratio

(+0.03 relative to **11** and +0.08 relative to **16**). The $E(T_2)/E(T_1)$ ratio of **17** was found to be the same as that of **11**, 0.02 smaller than calculated for **16**. The orbital character and distribution of the frontier MOs of **17** closely resemble those of its mono-aminated equivalents, **11** and **16**, akin to an average of the two. Table 2 presents the major MO contributions of the $S_0 \rightarrow S_1$ and $S_0 \rightarrow S_2$ transitions with oscillator strengths above 0.01 for structures **10**-**17**. Overall, the substitution investigated here had only a minor effect on bond lengths. However, due to steric hindrance introduced by amination of positions 1, 8, and 10, structures **10**, **14**, **16**, and **17** saw significant deviation from planarity, as evidenced by the increased N(5)-C(6)-C(6')-N(5') and C(1)-C-C-C(10) dihedral angles (Tables 3 and S3).

Table 2. TD-DFT vertical excitation energies, oscillator strengths (f_{osc}>0.01), and MO contributions (>10%) of select $S_0 \rightarrow S_n$ transitions in aminated derivates **10**-**17**.

Structure	S_n	E (eV)	f_{osc}	MO contributions
10	S_1	2.46	0.060	HOMO-1→LUMO (23%), HOMO→LUMO (72%)
	S_2	2.87	0.157	HOMO-2→LUMO (70%), HOMO-1→LUMO (21%)
11	S_1	2.64	0.561	HOMO→LUMO (86%)
12	S_1	2.46	0.091	HOMO-1→LUMO (17%), HOMO→LUMO (79%)
13	S_1	2.15	0.155	HOMO→LUMO (89%)
	S_2	2.89	0.402	HOMO-1→LUMO (71%), HOMO→LUMO+1 (12%)
14	S_1	2.62	0.334	HOMO→LUMO (85%)
15	S_1	2.75	0.283	HOMO→LUMO (85%)
16	S_1	2.51	0.345	HOMO→LUMO (86%)
17	S_1	2.59	0.573	HOMO→LUMO (84%)
	S_2	2.87	0.163	HOMO-1→LUMO (58%), HOMO→LUMO+1 (26%)

Table 3. Select dihedral angles of ground-state planar biphe (**5**) and aminated derivatives. Optimized at the PBE0-D3(BJ)/def2-SVP level of theory in vacuum.

Structure	Dihedral angle (°)		
	N(5)-C(6)-C(6')-N(5')	C(1)-C-C-C(10)	C(1')-C-C-C(10')
5	0.1	0.0	0.0
10	3.6	13.1	0.3
11	0.1	0.3	0.0
12	0.1	0.1	0.0
13	0.5	0.7	0.1
14	7.1	3.2	3.9
15	0.1	0.4	0.0
16	0.5	14.6	0.5
17	0.3	14.3	0.5

Further chemical modification of aminated planar biphe analogues. Considering the presence of three unique Lewis basic nitrogens, protonation of the unsubstituted phenanthridinyl nitrogen of both **11** and **16** yielded the lowest energy ground states. In both cases, protonation at the imine-like nitrogen of the aminated phenanthridinyl subunit was calculated to yield a ground state about 0.1 eV higher in energy than the lowest-energy protonated structure, while protonation of the amine substituent generates a ground state roughly 1.9 eV higher in energy. Here, only the lowest

energy protonated structures are discussed. Protonation of both **11** and **16** significantly stabilized each of the excited states. Interestingly, protonation of **11** stabilized both T_1 and T_2 to a much greater extent than S_1, whereas protonation of **16** lowered the singlet state more than either of the triplets. Accordingly, the $E(S_1)/E(T_1)$ ratio of protonated (2-amino) planar biphe (**18**) is 0.33 greater than for the non-protonated **11**, while that of protonated (10-amino) planar biphe (**19**) is only a moderate 0.09 greater than the neutral **16**. The $E(T_2)/E(T_1)$ ratios of **11** and **16** also increased by 0.10 and 0.30, respectively, upon protonation. Methylation of the unsubstituted phenanthridinyl nitrogen of both **11** and **16** to form **20** and **21**, respectively, had very similar effects on the energetics to that of protonation. Likewise, the frontier MOs of **18** and **19** closely resemble **20** and **21**, respectively (Figure S7). Like their neutral equivalents, **11** and **16**, the $S_0 \rightarrow S_1$ transition of the protonated species **18** and **19** are dominated by the frontier MOs (87% and 91% HOMO→LUMO, respectively). Similarly, the first transition of **21** is 92% HOMO→LUMO in character, but that of **20** is only 53% HOMO→LUMO and 37% HOMO-1→LUMO.

Replacing the amino group of **11** or **16** with a more electron-donating dimethylamino group to form 2-dimethylamino- (**22**) or (10-dimethylamino) planar biphe (**25**) reduced the $E(S_1)/E(T_1)$ ratio in these structures by 0.05 and 0.04, respectively. The $E(T_2)/E(T_1)$ ratio of **11** minimally increased by 0.01, while that of **16** decreased by 0.06. Protonation of **22** or **25** at the unsubstituted phenanthridinyl nitrogen caused substantial increases in both ratios {$\Delta[E(S_1)/E(T_1)] = +0.46$, $\Delta[E(T_2)/E(T_1)] = +0.19$ in **23** compared to **22**; $\Delta[E(S_1)/E(T_1)] = +0.18$, $\Delta[E(T_2)/E(T_1)] = +0.42$ in **26** compared to **25**}. Methylation at the unsubstituted phenanthridinyl nitrogen of **22** to form **24** increased $E(T_2)/E(T_1)$ to a smaller extent compared to protonation (**23**), whereas the *N*-methylated **27** had energetics nearly identical to protonated **26**. The $S_0 \rightarrow S_1$ transition of structures **22**-**27** is

dominated by the HOMO→LUMO excitation (**22**: 87%; **23**: 85%; **24**: 88%; **25**: 84%; **26**: 92%; **27**: 92%). The isosurfaces of these MOs are provided in Figures S8 and S9.

Electron withdrawing group substitution. Examining the results for 2- and 10-trifluoromethyl substituted planar biphe (**28** and **29**, respectively), it is clear that electron-withdrawing effects through induction alone do not significantly affect the excited state energies of **5**. Protonation of **28** to form **30** stabilized each of S_1, T_1 and T_2, but, overall, changes in the energetic ratios were insignificant. Installation of nitro substituents, on the other hand, led to a higher degree of stabilization of these excited states compared to trifluoromethyl groups, and both 2- and 10-nitro substituted planar biphe (**31** and **32**, respectively) have lower calculated gas-phase $E(S_1)/E(T_1)$ ratios compared with **28**/**29** due to a greater stabilization of the S_1 state than of T_1 or T_2. The first major excitation of the neutral trifluoromethyl substituted analogues **28** and **29** is calculated to be the $S_0 \rightarrow S_2$ transition and is largely defined by the HOMO→LUMO transition (84% and 87%, respectively). Similarly, the strong $S_0 \rightarrow S_1$ transition of the protonated analogue **30** is 82% HOMO→LUMO. The first excitation of the nitro substituted structures is also mostly characterized by the HOMO→LUMO transition (**31**: 85%; **32**: 70%), yet that of **32** also involves significant HOMO→LUMO+1 character (19%). The isosurfaces of these MOs are provided in Figures S10 and S11.

Electronic push-pull effects. Evolving **11** and **16** which bear electron-donating amino groups at the 2- and 10-positions, respectively, by adding electron-withdrawing trifluoromethyl or nitro groups at positions 2' and 10' produces eight disubstituted 'push-pull'-type structures (**33**-**40**). Of these, the nitro-substituted congeners (**34**, **36**, **38**, **40**) had lower excited state energies compared with their trifluoromethyl-substituted counterparts (**33**, **35**, **37**, **39**). However, the $E(S_1)/E(T_1)$ ratio was more affected by the *position* of substitution rather than the choice of electron withdrawing

group; $E(S_1)/E(T_1)$ is greatest when the EWG and EDG are directly opposite one another in the dimer as in **33**-**36** (**33**: 1.45; **34**: 1.44; **35**: 1.43; **36**: 1.46) compared to in **37**-**40** (**37**: 1.41; **38**: 1.33; **39**: 1.39; **40**: 1.32). On the other hand, **36** and **38** had the lowest $E(T_2)/E(T_1)$ ratios (1.35 and 1.36, respectively), while **40** had the highest $E(T_2)/E(T_1)$ at 1.48. Overall, however, the impact of 'push-pull' substitution patterns was rather minimal and the important energy ratios in **33**-**40** do not differ that significantly from the values for **11** or **16**. Like **11** and **16**, the $S_0 \rightarrow S_1$ excitation in the 'push-pull'-type structures is mostly characterized by the HOMO→LUMO transition (**33**: 87%; **34**: 90%; **35**: 85%; **36**: 88%; **37**: 86%; **38**: 81%; **39**: 88%; **40**: 90%). As seen in the MO isosurfaces (Figures S12 and S13), the HOMO→LUMO transition does not have significant CT character.

***N*-Oxide substitution.** Oxidizing one of the phenanthridinyl nitrogens of **5** *in silico* to form (5-*N*-oxide) planar biphe (**41**) caused substantial reduction of the excited state energies (T_1 = 1.57 eV, S_1 = 2.24 eV, T_2 = 1.97 eV), however, the energetic ratios were also slightly reduced ($\Delta E(S_1)/E(T_1)$ = -0.03; $\Delta E(T_2)/E(T_1)$ = -0.04). When the same modification was added to **22** to form (2-dimethylamino-5'-*N*-oxide) planar biphe (**42**), moderate improvement was observed in the $E(S_1)/E(T_1)$ ratio (+0.15) along with significant stabilization of the excited states, however the $E(T_2)/E(T_1)$ ratio was slightly lower in **42** compared to **22** (-0.05). Both the $S_0 \rightarrow S_1$ and $S_0 \rightarrow S_2$ excitation of **41** are predicted to be quite weak. The stronger $S_0 \rightarrow S_2$ excitation of **42** is attributed to a mix of HOMO→LUMO (43%), HOMO→LUMO+1 (28%), and HOMO-1→LUMO (19%) character. These MOs are depicted in Figure S14. Besides modification at the phenanthridinyl nitrogen, selective atomic replacement of ring carbons with *N*-oxide groups was also investigated. Addition of an *N*-oxide group to the 2' position of **22** to form **44** moderately improved $E(S_1)/E(T_1)$ (+0.11), while the $E(T_2)/E(T_1)$ ratio was not significantly affected. The doubly substituted (2,2'-di-*N*-oxide) planar biphe (**43**) was found to have a fairly high $E(S_1)/E(T_1)$ ratio (1.70) with a

corresponding improvement to $E(T_2)/E(T_1)$ relative to **5** (+0.15). Tetrasubstitution of **5** to form (2,2',10,10'-tetra-*N*-oxide) planar biphe (**45**) caused dramatic reduction in the excitation energies, nearly doubling the stabilization observed in **43** relative to **5**, resulting in an $E(S_1)/E(T_1)$ ratio greater than 2 (2.08) and a considerably high $E(T_2)/E(T_1)$ (1.61; see Figure S15 for MO isosurfaces). To support this finding, we benchmarked our level of theory by reproducing the results of Pradhan' and Zeng's higher-level calculations of the vertical excitation energies of the related chromophore, pyrazino[2,3-*g*]quinoxaline-1,4,6,9-tetraoxide (see reference for full computational details).[38] Comparing the reported values with those calculated at the RIJCOSX-TD-O3LYP/def2-TZVP + def2/J//PBE0-D3(BJ)/def2-SVP level of theory, absolute errors of the triplet states are small (ΔT_1 = -0.03 eV; ΔT_2 = -0.05 eV), while S_1 is significantly underestimated in our lower-level calculation (ΔS_1 = -0.16 eV). Consequently, the critical energetic ratios are comparatively underestimated ($E(S_1)/E(T_1)$ = 2.13 compared to 2.22; $E(T_2)/E(T_1)$ = 1.26 compared to 1.27), but modelling pyrazino[2,3-*g*]quinoxaline-1,4,6,9-tetraoxide at our level of theory does maintain an $E(S_1)/E(T_1)$ ratio greater than 2. By this reasoning, it is likely that **45** also satisfies the requirement $E(S_1)/E(T_1) \geq 2$.

Table 4 contains the single point energies of the optimized $T_{1,eq}$ and $S_{1,eq}$ excited states, T_1 at the S_1 optimized geometry ($T_1@S_{1,eq}$), and T_2 at the T_1 optimized geometry ($T_2@T_{1,eq}$) (all with respect to the ground state, $E(S_{0,eq})$ = 0 eV), along with the vertical excitation energies of the transitions $S_0 \rightarrow T_1$ ($T_1@S_{0,eq}$), $S_0 \rightarrow S_1$ ($S_1@S_{0,eq}$), and $S_0 \rightarrow T_2$ ($T_2@S_{0,eq}$) of **45**. By calculating the minimum-to-minimum excitation energies for T_1 and S_1, we obtain an $E(S_1)/E(T_1)$ ratio of 2.40. Utilizing the T_1 energy calculated at the S_1 geometry to account for vibrational relaxation of the S_1 excited state preceding SF, this ratio becomes 2.12. Similarly, the energy of the T_2 state calculated at the T_1 geometry (which may better model $T_1 + T_1 \rightarrow T_2 + S_0$ triplet fusion) leads to an

$E(T_2)/E(T_1)$ ratio of 2.05. The $\{T_1 + T_1 \rightarrow T_2 + S_0\}$ triplet fusion process is therefore slightly endoergic (0.04 eV), further suggesting the potential of **45** as a SF chromophore. Determining the T_2 energy at the T_1 geometry to more accurately model this process did not significantly change the energy compared to the value calculated at the ground-state geometry. In structures **43**-**45**, the $S_0 \rightarrow S_1$ excitation predominantly involves the HOMO→LUMO transition (**43**: 75%; **44**: 82%; **45**: 73%). Additionally, in structure **43**, there is a notable 15% contribution from the HOMO→LUMO+1 transition. The isosurfaces of these MOs are shown in Figure S15.

Table 4. Calculated excited state energies of **45** in vacuum.

State	Energy (eV)
$S_{0,eq}$	0.00
$T_1@S_{0,eq}$	1.07
$T_{1,eq}$	**0.90**
$T_1@S_{1,eq}$	**1.01**
$T_2@S_{0,eq}$	1.72
$T_2@T_{1,eq}$	**1.83**
$S_1@S_{0,eq}$	2.21
$S_{1,eq}$	**2.15**

Expanding and contracting the π-system of planar biphe. Monobenzannulation of the bay region between carbons 1 and 10 of **5** to form **46** stabilized the T_1, S_1, and T_2 states by 0.31, 0.23, and 0.05 eV, respectively, moderately improving both energetic ratios ($E(S_1)/E(T_1)$ = 1.58; $E(T_2)/E(T_1)$ = 1.50). Symmetric dibenzannulation between both carbons 1/10 and 1'/10' of **5** to form **47** further stabilized each excited state and further increased the $E(S_1)/E(T_1)$ and $E(T_2)/E(T_1)$ ratios to 1.67 and 1.61, respectively. Monobenzannulation of **47** at carbons 2 and 3 to form **48** significantly raised the T_1 state (+0.39 eV) while only slightly raising S_1 (+0.09 eV) and lowering T_2 (-0.10 eV) relative to **47**, leading to a reduction in the $E(S_1)/E(T_1)$ and $E(T_2)/E(T_1)$ ratios to 1.36 and 1.21, respectively. Symmetric dibenzannulation of **47** at carbons 2/3 and 2'/3' produces **49**, which has further stabilized excited states, minimally improving $E(S_1)/E(T_1)$ (1.40) and $E(T_2)/E(T_1)$ (1.22) relative to **48**. Combining dibenzannulation at carbons 2/3 and 2'/3' with bay benzannulation at carbons 1/10 of **5** leads to the asymmetric **50**, while with dibenzannulation at carbons 1/10 and 1'/10' leads to the symmetric **51**. Both structures bear significantly improved energetic ratios relative to **5** (**50**: $E(S_1)/E(T_1)$ = 1.60 and $E(T_2)/E(T_1)$ = 1.37; **51**: $E(S_1)/E(T_1)$ = 1.76 and $E(T_2)/E(T_1)$ = 1.56). In all cases, symmetrically benzannulated structures had larger energetic ratios compared to their asymmetric counterparts. Contracting the π-system by removing carbons 1, 2, 3, and 4 of **5**, on the other hand, to give **52** reduced the T_1 and S_1 states by 0.08 and 0.02 eV, respectively. This slightly improved both energetic ratios relative to **5** ($E(S_1)/E(T_1)$ = 1.50; $E(T_2)/E(T_1)$ = 1.35). Symmetric contraction of **5** to give 1,12-diazaperylene (**53**) effectively doubled this reduction of the excited state energies, further improving $E(S_1)/E(T_1)$ and $E(T_2)/E(T_1)$ to 1.56 and 1.42, respectively. Table 5 contains the MO contributions of the $S_0 \rightarrow S_1$ and $S_0 \rightarrow S_2$ transitions with oscillator strengths exceeding 0.001 for structures **46**-**53**. MO isosurfaces for selected orbitals of these structures are shown in Figures S16 and S17.

Table 5. TD-DFT vertical excitation energies, oscillator strengths (f_{osc}>0.001), and MO contributions (>10%) of select $S_0 \rightarrow S_n$ transitions in benzannulated and contracted structures **46**-**53**.

Structure	S_n	E (eV)	f_{osc}	MO contributions
46	S_1	2.65	0.583	HOMO→LUMO (87%)
47	S_1	2.43	0.680	HOMO→LUMO (89%)
48	S_1	2.52	0.083	HOMO-1→LUMO (40%), HOMO→LUMO (48%)
	S_2	2.81	0.627	HOMO-1→LUMO (43%), HOMO→LUMO (45%)
49	S_1	2.45	0.128	HOMO-2→LUMO (30%), HOMO→LUMO (61%)
50	S_1	2.34	0.089	HOMO-1→LUMO (79%), HOMO→LUMO (10%)
	S_2	2.36	0.492	HOMO→LUMO (76%)
51	S_1	2.17	0.728	HOMO→LUMO (90%)
52	S_2	2.96	0.549	HOMO→LUMO (89%)
53	S_2	3.19	0.001	HOMO-2→LUMO (99%)

Solvation. A previous study that used TD-DFT to screen for SF chromophores found that the $E(T_2)/E(T_1)$ ratio is not significantly affected when the implicit solvation model COSMO is employed.[40] We sought to verify this assumption as it applies to the various structural analogues of **2** using the implicit solvation model SMD,[24] with solvents chosen so as to cover a broad range of dielectric constants: chloroform (4.8), methanol (33.0), dimethyl sulfoxide (DMSO) (47.2), and water (78.4).[41] The structures chosen for this analysis were **4** (a cationic non-planar structure with representatively low $E(S_1)/E(T_1)$ and $E(T_2)/E(T_1)$ ratios in vacuum), **5** (a non-substituted planar structure chosen as the standard), **6** (a cationic planar structure with similar energetics to that of **5**), **23** and **24** (cationic EDG-substituted structures with representatively high $E(S_1)/E(T_1)$ and $E(T_2)/E(T_1)$ ratios in vacuum), **33** (a 'push-pull'-type structure), **42** (an EDG- and *N*-oxide-substituted structure), **43** (a symmetric di-*N*-oxide-substituted structure), and **45** (a symmetric tetra-*N*-oxide-substituted structure). The calculated energies of these solvated structures are presented in Table 6. It should be noted that these molecules are expected to exhibit very different photophysical properties in concentrated solutions or the solid state compared to their behaviour in dilute solution, primarily due to π-π stacking interactions (aggregation).

Table 6. Calculated excited state energies and their ratios of select structures in vacuum and solvent.

		$E(T_1)$ / eV	$E(S_1)$ / eV	$E(T_2)$ / eV	$\frac{E(S_1)}{E(T_1)}$	$\frac{E(T_2)}{E(T_1)}$
4	vacuum	2.42	2.46	2.45	1.01	1.01
	chloroform	2.76	2.82	2.82	1.02	1.02
	methanol	2.78	2.93	2.91	1.05	1.05
	DMSO	2.78	2.94	2.91	1.06	1.05
	water	2.78	2.94	2.90	1.06	1.04
5	vacuum	1.98	2.88	2.56	1.45	1.29
	chloroform	1.96	2.71	2.68	1.38	1.37
	methanol	1.94	2.70	2.66	1.39	1.37
	DMSO	1.94	2.68	2.66	1.38	1.37
	water	1.94	2.69	2.66	1.39	1.37
6	vacuum	1.62	2.35	2.06	1.45	1.27
	chloroform	1.66	2.29	2.20	1.38	1.32
	methanol	1.68	2.32	2.24	1.38	1.34
	DMSO	1.68	2.31	2.25	1.37	1.34

	water	1.67	2.32	2.25	1.38	1.34
	vacuum	1.24	2.30	2.00	1.86	1.62
	chloroform	1.23	2.09	2.03	1.71	1.65
23	methanol	1.22	2.13	2.03	1.75	1.67
	DMSO	1.22	2.10	2.04	1.72	1.67
	water	1.22	2.13	2.03	1.75	1.67
	vacuum	1.28	2.35	1.97	1.84	1.55
	chloroform	1.25	2.13	2.00	1.70	1.60
24	methanol	1.24	2.17	2.01	1.75	1.62
	DMSO	1.24	2.14	2.01	1.72	1.62
	water	1.24	2.17	2.01	1.75	1.62
	vacuum	1.80	2.61	2.55	1.45	1.42
	chloroform	1.70	2.40	2.46	1.41	1.45
33	methanol	1.65	2.39	2.42	1.45	1.47
	DMSO	1.64	2.36	2.41	1.44	1.47
	water	1.65	2.39	2.41	1.45	1.46

	vacuum	1.46	2.26	2.01	1.56	1.38
	chloroform	1.43	2.25	2.16	1.58	1.51
42	methanol	1.42	2.24	2.23	1.58	1.57
	DMSO	1.40	2.24	2.18	1.59	1.55
	water	1.40	2.22	2.22	1.59	1.58
	vacuum	1.46	2.49	2.10	1.70	1.44
	chloroform	1.52	2.43	2.16	1.60	1.42
43	methanol	1.61	2.47	2.28	1.53	1.42
	DMSO	1.51	2.43	2.15	1.61	1.42
	water	1.61	2.46	2.29	1.53	1.42
	vacuum	1.07	2.21	1.72	2.08	1.61
	chloroform	1.13	2.06	1.79	1.82	1.58
45	methanol	1.22	2.09	1.89	1.71	1.54
	water	1.23	2.08	1.89	1.70	1.54

The excited state energies (T_1, S_1, T_2) of **4** all increased upon solvation. While the energies in methanol, DMSO, and water were very similar, they differed from that in chloroform, which yielded lower-energy S_1 and T_2 states. Overall, the $E(S_1)/E(T_1)$ and $E(T_2)/E(T_1)$ ratios of **4**

increased slightly upon solvation, but more so in the higher-polarity solvents. In **5**, a small degree of stabilization of the T_1 energy was observed upon solvation and among the different solvents, while there was a moderate stabilization of S_1 and a moderate destabilization of T_2 among all the solvents. Each solvent yielded nearly identical $E(S_1)/E(T_1)$ and $E(T_2)/E(T_1)$ ratios for **5**, with a reduced $E(S_1)/E(T_1)$ and a moderately improved $E(T_2)/E(T_1)$ compared to that in vacuum. **6** saw a small increase in the T_1 energy, a small decrease in the S_1 energy, and moderate increase in T_2 across all solvents relative to vacuum, leading to a decreased $E(S_1)/E(T_1)$ and an increased $E(T_2)/E(T_1)$ upon solvation. The two triplet excited states of **23** were largely unaffected by solvation, with a very slight decrease of T_1 and increase of T_2. The S_1 of **23** saw a comparatively moderate decrease in energy upon solvation; thus, the $E(S_1)/E(T_1)$ ratio decreased significantly, while $E(T_2)/E(T_1)$ improved slightly. Like in **23**, a small decrease in the T_1 energy and a small increase in T_2 was observed in **24** upon solvation, along with a moderate decrease in S_1, again yielding a decreased $E(S_1)/E(T_1)$ ratio and an increased $E(T_2)/E(T_1)$. **33** saw a moderate decrease of both triplet states and an even greater decrease of S_1. Overall, there was minimal change in the $E(S_1)/E(T_1)$ of **33** in methanol, DMSO, and water, but this ratio was slightly lower in chloroform; the $E(T_2)/E(T_1)$ ratio improved slightly in all the solvents. The T_1 and S_1 states of **42** experienced small decreases in energy upon solvation, while the T_2 state increased moderately, leading to a slight increase of the $E(S_1)/E(T_1)$ ratio and a more moderately improved $E(T_2)/E(T_1)$. In **43**, the two triplet excited states increased slightly upon solvation by chloroform and DMSO and increased more moderately in methanol and water. The S_1 state, on the other hand, experienced a small decrease in energy in chloroform and DMSO, but very little decrease in methanol and water relative to **43** in vacuum. Accordingly, the $E(S_1)/E(T_1)$ ratio of **43** decreased significantly in all solvents, particularly in methanol and water, while there was a very small, uniform decrease in

$E(T_2)/E(T_1)$ across the different solvents. The two triplet excited states of **45** underwent changes in energy that closely paralleled those of **43** upon solvation. However, the S_1 state of solvated **45** saw a moderate decrease in energy relative to that in vacuum, yielding a much lower $E(S_1)/E(T_1)$ ratio and a significantly decreased $E(T_2)/E(T_1)$. Although **4**, a structure more suitable for TADF than SF, and **42** saw slight increases to the $E(S_1)/E(T_1)$ ratio, most presented more unfavourable values in dilute solution compared to those in vacuum. Furthermore, while most species exhibited greater $E(T_2)/E(T_1)$ ratios in solvent, the symmetrically substituted *N*-oxide analogues, particularly the promising **45**, suffered from reductions in both critical energetic ratios.

CONCLUSIONS

DFT and TD-DFT methods were used to predict the energies of the lowest excited singlet and triplet states of various structural analogues of 6,6'-biphenanthridine (biphe). The effects of chemical modifications made to biphe *in silico* on the critical energetic ratios $E(S_1)/E(T_1)$ and $E(T_2)/E(T_1)$ were investigated in an effort to find structures suitable for SF, as well as to identify general strategies for increasing these ratios. In total, imine protonation or *N*-methylation of 2-amino-substituted planar biphe were found to significantly increase the $E(S_1)/E(T_1)$ ratio. The analogue (2,2',10,10'-tetra-*N*-oxide) planar biphe (**45**) was found to have an $E(S_1)/E(T_1)$ value of 2.12 and an $E(T_2)/E(T_1)$ of 2.05, and may therefore be capable of SF. On the opposite end of the spectrum, *N*-methylated biphe (**4**) was identified as a promising candidate for thermally activated delayed fluorescence (TADF), having both a $\Delta E_{S1\text{-}T1}$ and $\Delta E_{S1\text{-}T2}$ smaller than 0.05 eV. Finally, the effects of solvation on the $E(S_1)/E(T_1)$ and $E(T_2)/E(T_1)$ ratios were found to be highly system dependent, with a tendency of $E(S_1)/E(T_1)$ to decrease and of $E(T_2)/E(T_1)$ to increase in a dielectric medium relative to gas-phase calculations.

SUPPORTING INFORMATION

A PDF containing selected MO isosurfaces; MO contributions to the $S_0 \rightarrow S_1$ and $S_0 \rightarrow S_2$ transitions; bond lengths; dihedral angles of ground-state optimized geometries; and coordinates.

CRediT Authorship Contribution Statement

Keighlynn A. Veilleux: investigation; formal analysis; validation; visualization; writing – original draft; writing – review & editing

Georg Schreckenbach: conceptualization; funding acquisition; supervision; project administration; writing – review & editing

David E. Herbert: conceptualization; funding acquisition; resources; supervision; project administration; writing – review & editing

CONFLICT OF INTEREST

The authors have no conflicts of interest to declare.

ACKNOWLEDGEMENTS

We are grateful to the Natural Sciences and Engineering Research Council of Canada for financial support of this work (DEH: RGPIN-2022-04501; GS: RGPIN-2023-04922) as well as to Compute Canada/Digital Research Alliance of Canada for computational resources. We also thank the Faculty of Science and the Science Student's Association at the University of Manitoba for a USRA fellowship to KAV.

REFERENCES

1 W. Shockley and H. J. Queisser, *J. Appl. Phys.*, 1961, **32**, 510–519.
2 M. B. Smith and J. Michl, *Chem. Rev.*, 2010, **110**, 6891–6936.
3 D. N. Congreve, J. Lee, N. J. Thompson, E. Hontz, S. R. Yost, P. D. Reusswig, M. E. Bahlke, S. Reineke, T. Van Voorhis and M. A. Baldo, *Science*, 2013, **340**, 334–337.
4 N. J. Thompson, D. N. Congreve, D. Goldberg, V. M. Menon and M. A. Baldo, *Appl. Phys. Lett.*, 2013, **103**, 263302.
5 K. E. Smyser and J. D. Eaves, *Sci. Rep.*, 2020, **10**, 18480.
6 Y. Kawashima, T. Hamachi, A. Yamauchi, K. Nishimura, Y. Nakashima, S. Fujiwara, N. Kimizuka, T. Ryu, T. Tamura, M. Saigo, K. Onda, S. Sato, Y. Kobori, K. Tateishi, T. Uesaka, G. Watanabe, K. Miyata and N. Yanai, *Nat. Commun.*, 2023, **14**, 1056.
7 A. Japahuge and T. Zeng, *ChemPlusChem*, 2018, **83**, 146–182.
8 D. Casanova, *Chem. Rev.*, 2018, **118**, 7164–7207.
9 M. Kasha, *Discuss. Faraday Soc.*, 1950, **9**, 14.
10 A. Rao and R. H. Friend, *Nat. Rev. Mater.*, 2017, **2**, 17063.
11 V. Gray, J. R. Allardice, Z. Zhang, S. Dowland, J. Xiao, A. J. Petty, J. E. Anthony, N. C. Greenham and A. Rao, *ACS Nano*, 2020, **14**, 4224–4234.
12 K. Miyata, F. S. Conrad-Burton, F. L. Geyer and X.-Y. Zhu, *Chem. Rev.*, 2019, **119**, 4261–4292.
13 H. Kim and P. M. Zimmerman, *Phys. Chem. Chem. Phys.*, 2018, **20**, 30083–30094.
14 T. Wang, B. Zhang and H. Zhang, *Macromol. Rapid Commun.*, 2022, **43**, 2200326.
15 D. B. Nemez, I. B. Lozada, J. D. Braun, J. A. G. Williams and D. E. Herbert, *Inorg. Chem.*, 2022, **61**, 13386–13398.
16 L.-M. Tumir, M. R. Stojkovic and I. Piantanida, *Beilstein J. Org. Chem.*, 2014, **10**, 2930–2954.
17 T. C. Johnstone, G. Y. Park and S. J. Lippard, *Anticancer Res.*, 2014, **34**, 471–476.
18 Q.-A. Chen, K. Gao, Y. Duan, Z.-S. Ye, L. Shi, Y. Yang and Y.-Gui. Zhou, *J. Am. Chem. Soc.*, 2012, **134**, 2442–2448.
19 L.-Q. Lu, Y. Li, K. Junge and Matthias. Beller, *Angew. Chem., Int. Ed.*, 2013, **52**, 8382–8386.
20 D. E. Herbert, *Can. J. Chem.*, 2024, **101**, 892-902
21 F. Neese, *WIREs Comput. Mol. Sci.*, 2012, **2**, 73–78.
22 F. Neese, F. Wennmohs, U. Becker and C. Riplinger, *J. Chem. Phys.*, 2020, **152**, 224108.
23 F. Neese, *WIREs Comput. Mol. Sci.*, 2018, **8**, e1327
24 A. V. Marenich, C. J. Cramer and D. G. Truhlar, *J. Phys. Chem. B*, 2009, **113**, 6378–6396.
25 C. Adamo and V. Barone, *J. Chem. Phys.*, 1999, **110**, 6158–6170.
26 M. Ernzerhof and G. E. Scuseria, *J. Chem. Phys.*, 1999, **110**, 5029–5036.
27 A. D. Becke and E. R. Johnson, *J. Chem. Phys.*, 2005, **123**, 154101.
28 F. Weigend and R. Ahlrichs, *Phys. Chem. Chem. Phys.*, 2005, **7**, 3297.
29 A. J. Cohen and N. C. Handy, *Mol. Phys.*, 2001, **99**, 607–615.
30 F. Neese and G. Olbrich, *Chem. Phys. Lett.*, 2002, **362**, 170–178.
31 F. Neese, *J. Comput. Chem.*, 2003, **24**, 1740–1747.
32 F. Neese, F. Wennmohs, A. Hansen and U. Becker, *Chem. Phys.*, 2009, **356**, 98–109.
33 F. Weigend, *Phys. Chem. Chem. Phys.*, 2006, **8**, 1057.
34 S. Hirata and M. Head-Gordon, *Chem. Phys. Lett.*, 1999, **314**, 291–299.

35 M. J. G. Peach, M. J. Williamson and D. J. Tozer, *J. Chem. Theory Comput.*, 2011, **7**, 3578–3585.
36 G. A. Zhurko and D. A. Zhurko, Chemcraft - graphical program for visualization of quantum chemistry computations https://www.chemcraftprog.com/ 2005.
37 E. C. Greyson, J. Vura-Weis, J. Michl and M. A. Ratner, *J. Phys. Chem. B*, 2010, **114**, 14168–14177.
38 E. Pradhan and T. Zeng, *J. Phys. Chem. Lett.*, 2022, **13**, 11076–11085.
39 P. Data, P. Data and Y. Takeda, *Chem. Asian J.*, 2019, **14**, 1613–1636.
40 C. Match, J. Perkins and G. Schreckenbach, *Theor. Chem. Acc.*, 2018, **137**, 109.
41 W. M. Haynes, D. R. Lide and T. J. Bruno, *CRC Handbook of Chemistry and Physics*, CRC Press, Boca Raton, FL, 95th edn., 2014.